

# Anisotropic hyperfine interaction of surface-adsorbed single atoms

Jinkyung Kim,<sup>†,‡,§</sup> Kyungju Noh,<sup>†,‡,§</sup> Yi Chen,<sup>†,¶,§</sup> Fabio Donati,<sup>†,‡</sup> Andreas J.  
Heinrich,<sup>\*,†,‡</sup> Christoph Wolf,<sup>\*,†,¶</sup> and Yujeong Bae<sup>\*,†,‡</sup>

<sup>†</sup>*Center for Quantum Nanoscience (QNS), Institute for Basic Science (IBS), Seoul 03760,  
South Korea*

<sup>‡</sup>*Department of Physics, Ewha Womans University, Seoul 03760, South Korea*

<sup>¶</sup>*Ewha Womans University, Seoul 03760, Republic of Korea*

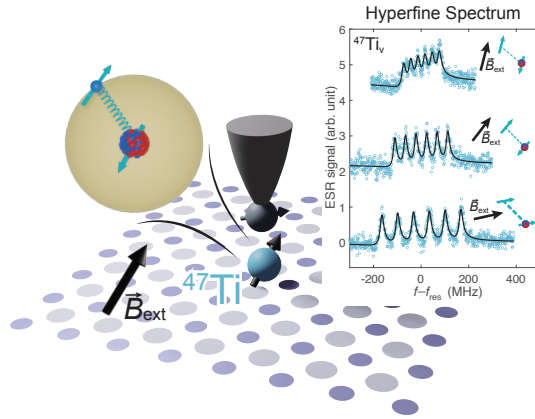
<sup>§</sup>*These authors contributed equally to this work.*

E-mail: heinrich.andreas@qns.science; wolf.christoph@qns.science; bae.yujeong@qns.science

## Abstract

Hyperfine interactions between electron and nuclear spins have been widely used in material science, organic chemistry, and structural biology as a sensitive probe to the local chemical environment through spatial identification of nuclear spins. With the nuclear spins identified, the isotropic and anisotropic components of the hyperfine interactions in turn offer unique insight into the electronic ground-state properties of the paramagnetic centers. However, traditional ensemble measurements of hyperfine interactions average over a macroscopic number of spins with different geometrical locations and nuclear isotopes. Here, we use a scanning tunneling microscope (STM) combined with electron spin resonance (ESR) to measure hyperfine spectra of hydrogenated-titanium (Ti) atoms on MgO/Ag(100) and thereby determine the isotropic and anisotropic hyperfine interactions at the single-atom level. By combining

vector-field ESR spectroscopy with STM-based atom manipulation, we characterize the full hyperfine tensor of individual  $^{47}\text{Ti}$  and  $^{49}\text{Ti}$  atoms and identify significant spatial anisotropy of hyperfine interaction for both isotopes when they are adsorbed at low-symmetry binding sites. Density functional theory calculations reveal that the large hyperfine anisotropy arises from a highly anisotropic distribution of the ground-state electron spin density. Our work highlights the power of ESR-STM-enabled single-atom hyperfine spectroscopy as a powerful tool in revealing ground-state electronic structures and atomic-scale chemical environments with nano-electronvolt resolution.



Keywords: Scanning tunneling microscopy, Electron spin resonance, Scanning probe, Hyperfine interaction, Nuclear spin

Conventional ensemble magnetic resonance techniques have been extensively used for probing hyperfine interactions between paramagnetic spin centers and nearby nuclear spins, where the sensitivity largely depends on the spin concentration.<sup>1</sup> Hyperfine interactions at the single spin level have recently attracted significant interests due to promise in sensitive detection of the local chemical environment<sup>2</sup> and nuclear-spin-based quantum information processing.<sup>3-6</sup> These new scientific endeavors are enabled by technological developments that allow electron spin resonance (ESR) operations at the single-spin level,<sup>7</sup> for example, through optically addressable color centers in insulators<sup>8,9</sup> or semiconductor donor atoms equipped with nanofabricated charge detectors.<sup>10</sup> However, for a general paramagnetic center placed

in its native chemical environment, characterization of the hyperfine interactions at the single-spin level has been extremely difficult.

Scanning tunneling microscopy (STM) with ESR capabilities offers a new appealing platform for *in-situ* characterization of individual spin-carrying atoms and molecules.<sup>11–13</sup> ESR-STM spectroscopy offers tens of nano-electrovolt energy resolution, far beyond traditional STM bias spectroscopy,<sup>14–16</sup> thus allowing for probing hyperfine interactions at the atomic scale.<sup>17,18</sup> When combined with STM’s single-atom selectivity, hyperfine interactions from single atoms with different isotopes and different binding sites can be individually determined without any spatial averaging.<sup>19</sup>

Here we use a state-of-the-art ESR-STM system to measure the full hyperfine tensor of single hydrogenated  $^{47}\text{Ti}$  and  $^{49}\text{Ti}$  atoms on  $\text{MgO}/\text{Ag}(100)$ . Using a vector magnetic field and STM-based atom manipulation, we quantify the isotropic and anisotropic hyperfine interactions for the two Ti isotopes. A large hyperfine anisotropy of more than 67% is observed for both Ti isotopes on a low-symmetry binding site, which reveals a highly anisotropic distribution of the ground-state spin density that is consistent with density functional theory (DFT) results.

We performed ESR-STM experiments using a home-built STM system equipped with RF cabling and a two-axis vector magnet.<sup>20</sup> The vector magnet provides an in-plane magnetic field up to 9 T and an out-of-plane field up to 2 T. Individual Ti atoms were deposited on two monolayers of  $\text{MgO}(100)$  grown on a  $\text{Ag}(100)$  substrate while the sample was kept below 10 K in the STM stage (Figure 1a). Evaporation of Ti was performed using a commercial electron-beam evaporator. Ti rods with natural isotope abundance were used, in which the most abundant isotope,  $^{48}\text{Ti}$ , has zero nuclear spin, while  $^{47}\text{Ti}$  (with 7.4% abundance) has a nonzero nuclear spin of  $I = 5/2$  and  $^{49}\text{Ti}$  (with 5.4% abundance) has a nuclear spin of  $I = 7/2$  (Figure 1b).<sup>21</sup> Due to the residual hydrogen gas in the vacuum chamber,<sup>22</sup> Ti atoms deposited on the  $\text{MgO}$  surface are most likely hydrogenated and are known to have electron spin-1/2.<sup>23,24</sup> Here, we denote the hydrogenated Ti atoms as Ti for simplicity. Ti atoms were

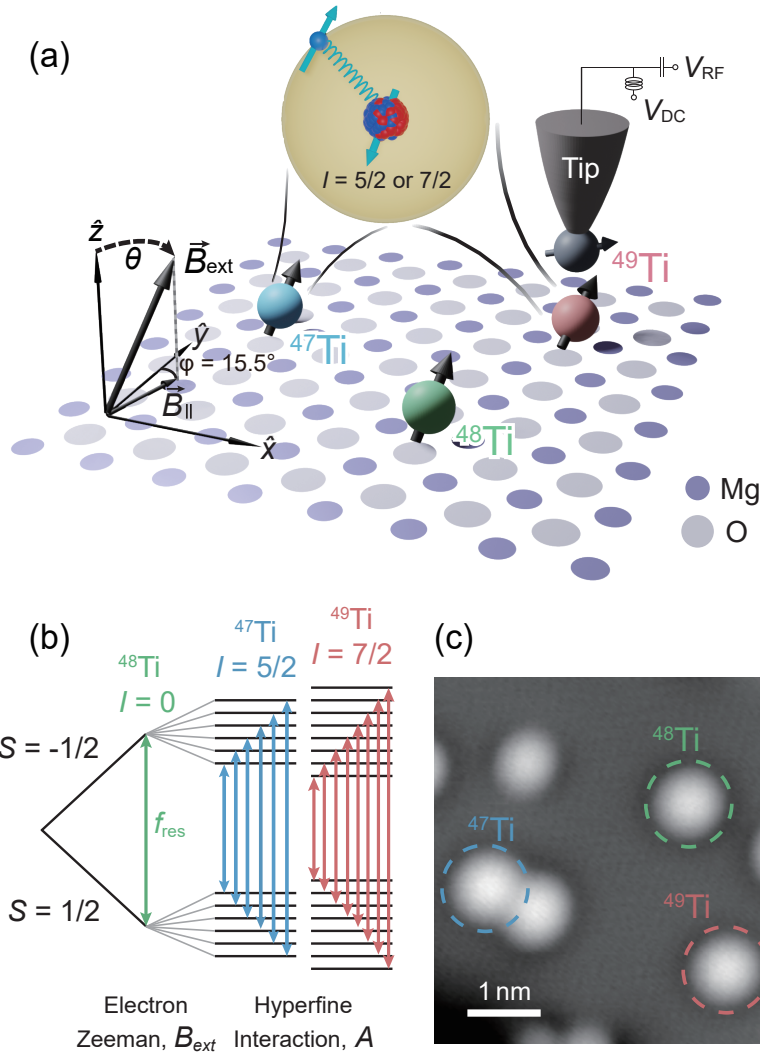


Figure 1: Hyperfine interaction of single hydrogenated titanium (Ti) atoms on the MgO/Ag(100) surface. (a) Schematic of the ESR-STM measurements on different isotopes of Ti under a rotatable magnetic field. Single-atom ESR spectroscopy is performed by detecting the change of spin-polarized tunnel current under resonant driving. The MgO lattice directions are indicated by  $\hat{x}$  and  $\hat{y}$ , whereas  $\hat{z}$  is the out-of-plane direction. A vector external magnetic field  $\mathbf{B}_{\text{ext}}$  is applied in a plane which is  $15.5^\circ$  rotated from the  $yz$ -plane around the  $\hat{z}$ -axis. The rotation angle of  $\mathbf{B}_{\text{ext}}$  relative to the out-of-plane direction is labelled as  $\theta$ . (b) Schematic of energy levels and ESR transitions of different Ti isotopes in the presence of a magnetic field  $B_{\text{ext}}$  and the hyperfine interaction  $A$ . The ESR transitions are denoted by double sided arrows. (c) STM image showing three different types of Ti isotopes. Different Ti isotopes show identical topographic features but can be readily identified through ESR spectroscopy (Figure 2 and S1) ( $V_{\text{DC}} = 100$  mV,  $I = 20$  pA).

found at two different types of binding sites on MgO(100), atop of an oxygen atom<sup>23,25</sup> or at a bridge site between two oxygen atoms.<sup>24,26</sup> In this work, we focus on Ti atoms at the bridge binding sites, which have a significantly larger hyperfine coupling than the oxygen binding sites.<sup>17</sup> Note that in our experimental set-up, the in-plane magnetic-field axis is  $15.5^\circ$  tilted from the oxygen lattice direction of MgO(100) (Figure 1a). This results in two non-identical bridge binding sites of Ti, referred to as Ti near the vertical direction ( $\text{Ti}_v$ ) and Ti near the horizontal direction ( $\text{Ti}_h$ ).<sup>20,27</sup> These two inequivalent in-plane sites, in combination with the two-axis magnetic field, allow us to determine the hyperfine interaction tensor as discussed below.

Figure 1c shows a typical STM image containing three different types of Ti isotopes. While Ti atoms with different isotopes show identical STM topographic and bias spectroscopic features, they are clearly distinguishable from STM-based ESR spectroscopy (Figure S1). Out of 94 Ti atoms that we measured, the majority (83 atoms) show only one ESR peak, corresponding to the most abundant  $^{48}\text{Ti}$  isotope with zero nuclear spin (Figure 1b and S1). 6 Ti atoms (roughly 6.4%) exhibit 6 ESR peaks that correspond to  $^{47}\text{Ti}$  with  $I = 5/2$ , and 5 Ti atoms (roughly 5.3%) exhibit 8 ESR peaks that correspond to  $^{49}\text{Ti}$  with  $I = 7/2$  (Figure 1b and S1). The hyperfine splitting is much smaller than the thermal energy at 0.6 K, resulting in nearly equal populations in the nuclear spin states and thus equal peak intensities. The ESR peaks observed in our measurements are found to be equally spaced (see, e.g., Figure 2 and S1), which indicates negligible contributions of the nuclear Zeeman interaction and the electric quadrupole interaction.<sup>28</sup> These considerations lead us to write down a simplified spin Hamiltonian of the  $^{47}\text{Ti}$  and  $^{49}\text{Ti}$  atoms as

$$\mathcal{H} = \mu_B \mathbf{B}_{\text{ext}} \cdot \mathbf{g} \cdot \mathbf{S} + \mathbf{S} \cdot \mathbf{A} \cdot \mathbf{I} = \mu_B \mathbf{B}_{\text{ext}} \cdot \mathbf{g} \cdot \mathbf{S} + A_{\text{iso}} \mathbf{S} \cdot \mathbf{I} + \mathbf{S} \cdot \mathbf{T} \cdot \mathbf{I}, \quad (1)$$

where  $\mathbf{S}$  and  $\mathbf{I}$  are the electron and nuclear spin operators, respectively,  $\mathbf{B}_{\text{ext}}$  is the external magnetic field, and  $\mathbf{g}$  is the electron  $g$ -tensor.  $\mathbf{A}$  is the tensor of hyperfine interaction that can

be decomposed into an isotropic contact term,  $A_{\text{iso}}$ , that originates from the direct overlap between the electronic wavefunction and the nuclear spin, and an anisotropic contribution,  $\mathbf{T}$ , that originates from dipolar interactions between the electron and nuclear spins.<sup>28</sup> The principal axes for  $\mathbf{g}$  and  $\mathbf{A}$  tensors coincide with the crystalline lattice axes of MgO to match the  $C_{2v}$  symmetry of Ti on bridge sites.<sup>28</sup>

Different components of the  $\mathbf{A}$  tensor can be probed by changing the direction of the external magnetic field  $\mathbf{B}_{\text{ext}}$ . Under the external magnetic field  $\mathbf{B}_{\text{ext}}$  of 0.8 T (which is used in all measurements shown in the main text), the electron Zeeman term of the Hamiltonian in eq. 1 dominates and determines the electron spin direction to be almost parallel with  $\mathbf{B}_{\text{ext}}$  (some deviation arises from  $\mathbf{g}$ -factor anisotropy<sup>20</sup>). The electron spin direction in turn determines the nuclear spin direction through the hyperfine coupling  $\mathbf{A}$ . The rotation of  $\mathbf{B}_{\text{ext}}$  thus rotates the electron spin  $\mathbf{S}$  and the nuclear spin  $\mathbf{I}$  together with it, allowing us to probe different components of  $\mathbf{A}$  through the term  $\mathbf{S} \cdot \mathbf{A} \cdot \mathbf{I}$ . The energy change associated with the hyperfine interaction,  $\mathbf{S} \cdot \mathbf{A} \cdot \mathbf{I}$ , is detected through the splitting between adjacent ESR peaks,  $\Delta f$ . For a Ti atom with  $S = 1/2$ , the ESR transition associated with a certain nuclear spin state,  $m_I$ , has a frequency of  $hf_{m_I} = \mu_B B_{\text{ext}} g(\theta) + A(\theta)m_I$ , where  $h$  is the Planck's constant and  $g(\theta)$  and  $A(\theta)$  are experimentally probed  $g$ -factor and hyperfine constant, respectively, at the field angle  $\theta$ . The frequency splitting between adjacent ESR lines thus directly yields the hyperfine interaction, since  $\Delta f = |f_{m_I} - f_{m_I \pm 1}| = A(\theta)$ . The relation between experimentally probed  $A(\theta)$  and the principal values of the  $\mathbf{A}$  tensor will be discussed later (see eq. 2).

Figure 2 shows the experimental results at different field angles. At  $\theta = -20^\circ$  (close to the out-of-plane direction, see Figure 1a), the ESR splittings for  $^{47}\text{Ti}_v$  (Figure 2a) and  $^{49}\text{Ti}_v$  (Figure 2b) are measured to be  $30.0 \pm 0.4$  MHz and  $29.0 \pm 0.3$  MHz, respectively. We find that the energy splittings  $\Delta f$  measured for  $^{47}\text{Ti}_v$  and  $^{49}\text{Ti}_v$  are equal within the uncertainty of our measurements, as expected from their identical electronic ground states and very similar nuclear magnetic moments.<sup>29</sup> The hyperfine interaction is significantly increased when we

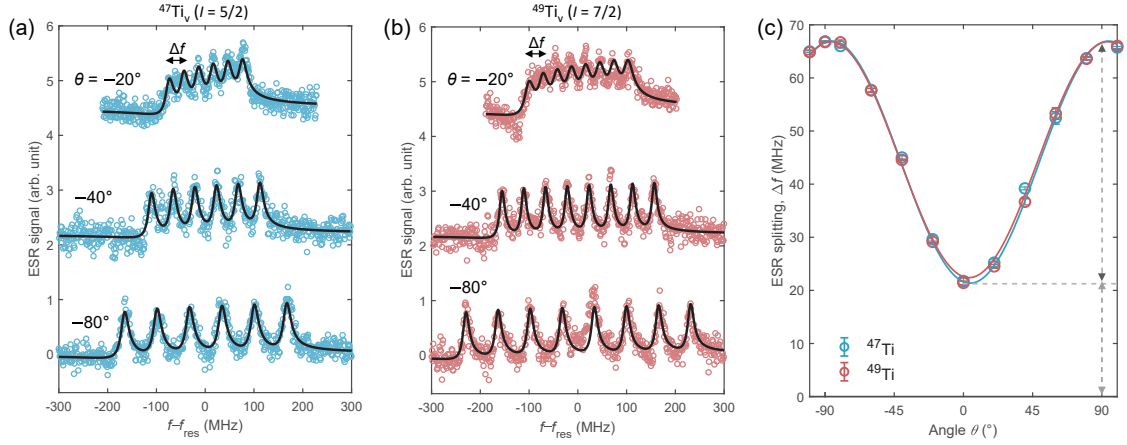


Figure 2: Angular variations of hyperfine interactions of  $^{47}\text{Ti}_v$  and  $^{49}\text{Ti}_v$ . (a) Hyperfine spectra of  $^{47}\text{Ti}_v$  and (b)  $^{49}\text{Ti}_v$  measured at different angles  $\theta$  of the external magnetic field. For both isotopes, the hyperfine splitting is greatly increased when the field is rotated away from the out-of-plane direction (i.e., for the shown data, towards more negative  $\theta$ ). Fits in (a) yield a hyperfine splitting of  $30.0 \pm 0.4$  MHz at  $\theta = -20^\circ$ ,  $44.4 \pm 0.3$  MHz at  $\theta = -40^\circ$ , and  $66.5 \pm 0.2$  MHz at  $\theta = -80^\circ$ . In (b), the hyperfine splitting is determined to be  $29.0 \pm 0.3$  MHz at  $\theta = -20^\circ$ ,  $44.6 \pm 0.1$  MHz at  $\theta = -40^\circ$ , and  $65.8 \pm 0.2$  MHz at  $\theta = -80^\circ$ . ESR spectra are plotted against  $f - f_0$ , where  $f_0$  is the resonance frequency of a  $^{48}\text{Ti}_v$  atom (with zero nuclear spin) measured under the same conditions. ESR spectra are normalized in intensity, and successive curves are vertically shifted for clarity ( $V_{\text{DC}} = 40$  mV,  $I_{\text{set}} = 1.5 \sim 8$  pA,  $V_{\text{RF}} = 15 \sim 50$  mV). (c) Hyperfine splittings of  $^{47}\text{Ti}_v$  and  $^{49}\text{Ti}_v$  measured as a function of the magnetic field angle,  $\theta$ . Solid curves are guides to the eye. Dashed arrows highlight the significant hyperfine anisotropy between in-plane and out-of-plane directions. Error bars are given by the standard errors of different measurements under the same conditions. From these measurements we conclude that there is no noticeable difference in the hyperfine splittings of  $^{47}\text{Ti}$  and  $^{49}\text{Ti}$ .

rotate the magnetic field closer to an in-plane direction as shown in Figure 2a, b. The large angular variations of the hyperfine splittings for  $^{47}\text{Ti}_v$  and  $^{49}\text{Ti}_v$  are summarized in Figure 2c. In both cases, the largest splitting of  $\sim 67$  MHz is observed at  $\theta \approx 90^\circ$  when  $\mathbf{B}_{\text{ext}}$  is applied along an in-plane direction, while the smallest splitting of  $\sim 22$  MHz is obtained along the out-of-plane direction. These observations indicate very large hyperfine anisotropy (around 67%, see Figure 2c) for both  $^{47}\text{Ti}_v$  and  $^{49}\text{Ti}_v$  atoms. Due to their nearly identical hyperfine interactions, we will focus on  $^{47}\text{Ti}$  in the following.

To determine the hyperfine interaction along the third axis that is not in the tunable plane of the external magnetic field (i.e., the  $x$  axis in Figure 1a), we exploit two inequivalent bridge binding sites of Ti on MgO ( $\text{Ti}_v$  and  $\text{Ti}_h$ ). Using atom manipulation, Ti atoms can be moved reversibly between different binding sites on MgO.<sup>23</sup> Figure 3a, b shows STM images of  $^{47}\text{Ti}_v$  and  $^{47}\text{Ti}_h$  taken before and after a typical atom manipulation. Strikingly, this manipulation significantly changes hyperfine spectra as shown in Figure 3c, d. With  $\mathbf{B}_{\text{ext}}$  applied along the out-of-plane direction (at  $\theta = 0^\circ$ ),  $\text{Ti}_v$  and  $\text{Ti}_h$  are at physically identical sites and exhibit very similar hyperfine spectra (upper curves in Figure 3c, d). With  $\mathbf{B}_{\text{ext}}$  applied along the in-plane direction, however, the large anisotropy observed in  $\text{Ti}_v$  is almost absent in  $\text{Ti}_h$  (lower curves in Figure 3c, d). This trend is clearly shown in Figure 3f where a large change of the hyperfine splitting is only observed for  $\text{Ti}_v$ . Since the in-plane field direction of  $\text{Ti}_v$  is almost aligned with the O-O direction (see inset of Figure 3c), this trend suggests that the hyperfine interaction along the O-O direction is significantly larger than the other two principal axes.

The extensive hyperfine spectra presented above allow us to quantitatively extract the hyperfine interactions along the three principal axes of bridge-site Ti atoms. Taking both  $\mathbf{A}$  and  $\mathbf{g}$ -factor anisotropies under consideration, the experimentally observed hyperfine splitting  $A(\theta)$  is related to its principal values by<sup>28</sup>

$$g(\theta)A(\theta) = \sqrt{l^2 g_{\text{O}}^2 A_{\text{O}}^2 + m^2 g_{\text{Mg}}^2 A_{\text{Mg}}^2 + n^2 g_z^2 A_z^2}, \quad (2)$$



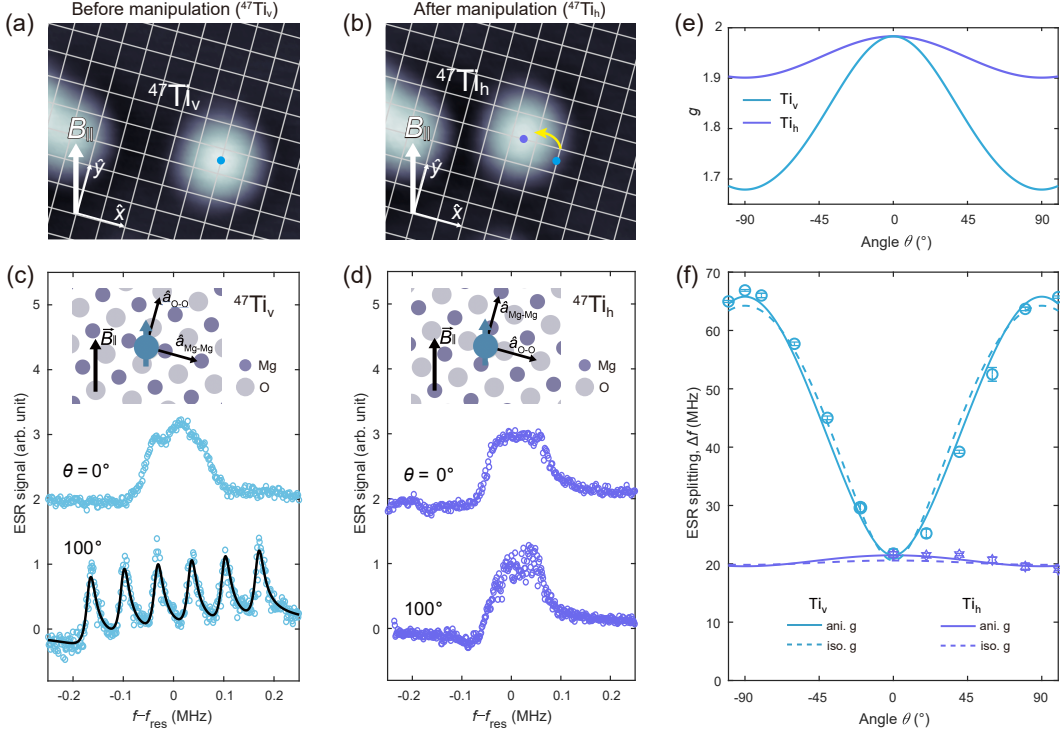


Figure 3: Binding-site-dependent hyperfine spectra of Ti atoms on MgO. (a) STM image of  $^{47}\text{Ti}$  at a vertical bridge binding site ( $^{47}\text{Ti}_v$ ). The intersection of grid lines corresponds to the location of oxygen atoms in the MgO lattice. (b) STM image of  $^{47}\text{Ti}_h$  taken after moving  $^{47}\text{Ti}_v$  in (a) by  $1.5 \times 0.5$  oxygen lattices, to the horizontal site. The white arrow in each STM image indicates the in-plane magnetic field direction ( $B_{\parallel}$ ) with respect to the MgO lattice (scan conditions:  $V_{\text{DC}} = 100$  mV,  $I = 20$  pA). (c) Hyperfine spectra of  $^{47}\text{Ti}_v$  and (d)  $^{47}\text{Ti}_h$ , measured at  $\theta = 0^\circ$  (upper) and  $100^\circ$  (lower). The curves are normalized to unity. Successive curves are vertically shifted for clarity ( $V_{\text{DC}} = 40$  mV,  $I = 12 \sim 20$  pA,  $V_{\text{RF}} = 15 \sim 20$  mV). Insets show that  $B_{\parallel}$  is close to the O-O direction for  $^{47}\text{Ti}_v$  and Mg-Mg direction for  $^{47}\text{Ti}_h$ . (e)  $g$ -factors of bridge-site Ti as a function of the angle  $\theta$  as calculated based on the anisotropic  $g$ -factors determined in ref.<sup>20</sup> (f) Anisotropic hyperfine coupling of  $^{47}\text{Ti}_v$  and  $^{47}\text{Ti}_h$  measured at different magnetic field angles. The O-O direction, close to the in-plane direction of  $^{47}\text{Ti}_v$ , shows a significantly higher hyperfine interaction strength than the other two principal axes. Solid and dashed curves correspond to fits to eq. 2 with anisotropic and isotropic  $g$ -values, respectively. The hyperfine splittings at small field angles in Figure 3f are obtained using a different STM tip that allows better resolution (see Figure S3).

where  $(l, m, n)$  are the direction cosines given by  $(l, m, n) = (\sin \theta \cos \varphi, \sin \theta \sin \varphi, \cos \theta)$  and  $g(\theta) = (l^2 g_{\text{O}}^2 + m^2 g_{\text{Mg}}^2 + n^2 g_z^2)^{1/2}$ . In our setup,  $\varphi_{\text{h}} = 15.5^\circ$  and  $\varphi_{\text{v}} = 105.5^\circ$  for  $^{47}\text{Ti}_{\text{v}}$  and  $^{47}\text{Ti}_{\text{h}}$ , respectively. Using the  $g$ -factors that we measured before on bridge-site Ti,  $(g_{\text{O}}, g_{\text{Mg}}, g_z) = (1.653, 1.917, 1.989)$  (Figure 3e),<sup>20</sup> the best fits to the hyperfine splittings (solid curves Figure 3f) yield three principal values of hyperfine interaction tensor,  $(A_{\text{O}}, A_{\text{Mg}}, A_z) = (68.97 \pm 1.23, 11.66 \pm 3.59, 21.23 \pm 1.52)$ . These results indicate a significantly larger hyperfine interaction along the O-O axis compared to the other two axes (Mg-Mg and out-of-plane directions), agreeing with the trends in Figure 3f. The  $g$ -factor anisotropy is not important in determining the hyperfine constants, as shown by very similar fitting results assuming an isotropic  $g$ -factor of 2.003 (dashed curves in Figure 3f). The complete determination of the hyperfine tensor  $\mathbf{A}$  allows us to calculate its isotropic and anisotropic components (see eq. 1). Since the dipolar hyperfine tensor  $\mathbf{T}$  is traceless, the isotropic hyperfine interaction can be determined experimentally to be  $A_{\text{iso}} = 1/3\text{Tr}(\mathbf{A}) = 33.95 \pm 1.36$  MHz. The dipolar hyperfine tensor  $\mathbf{T}$  is then obtained by subtracting  $A_{\text{iso}}$  from  $\mathbf{A}$ , resulting in  $(T_{\text{O}}, T_{\text{Mg}}, T_z) = (35.02 \pm 1.84, -22.29 \pm 3.84, -12.72 \pm 2.04)$  MHz.

The observed large hyperfine anisotropy along the O-O direction uniquely reflects a highly anisotropic ground-state wavefunction of bridge-site Ti atoms. This is shown by DFT calculations using the GIPAW formalism implemented in Quantum Espresso.<sup>30,31</sup> Our model consists of 4 layers of Ag capped by two layers of MgO and a hydrogenated Ti atom adsorbed on a bridge site (Figure 4a and S7). The resulting DFT ground-state is a mixture of  $s$ ,  $d_{yz}$ , and  $d_{x^2-y^2}$  orbitals, and its spin-polarization isosurface is shown in Figure 4a. We found that the isotropic hyperfine interaction,  $A_{\text{iso}}$ , is positive and dominates over the dipolar contribution,  $T$ . As a result, the electron and nuclear spins of Ti are always anti-aligned, and the same holds for their magnetic moments as shown in the upper row of Figure 4b-d (note that the  $g$ -factors of both the electron and nuclear spins of Ti are negative). The large hyperfine anisotropy along the O-O direction arises from the highly anisotropic ground-state spin distribution (mostly concentrated in the plane spanned by Mg-Mg and  $\hat{z}$  directions,

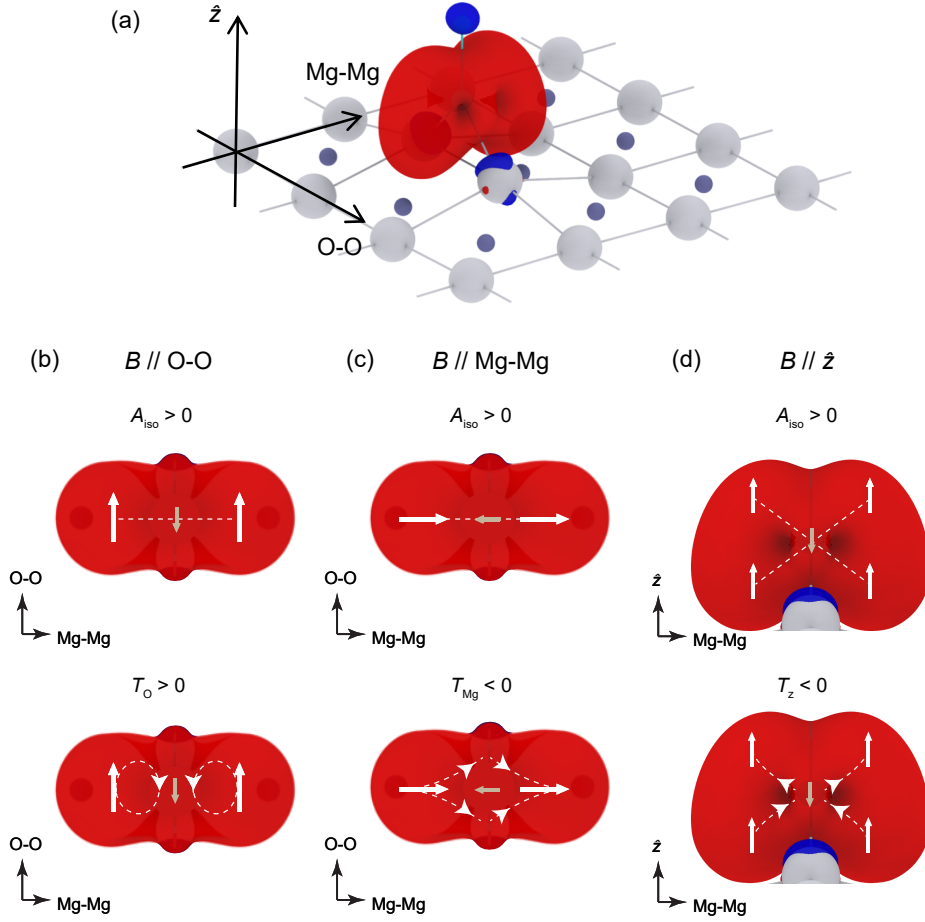


Figure 4: DFT calculations of the spin distribution and hyperfine interactions of bridge-site Ti on MgO. (a) Isometric view of Ti on MgO/Ag with only the top layer of MgO shown for clarity. The red (blue) isosurfaces represent the positive (negative) electron spin polarization (isovalue = 0.002 electrons/ $a_0^3$ ). (b–d) Schematics of isotropic and anisotropic hyperfine interactions with  $\mathbf{B}_{\text{ext}}$  applied along the three principal axes. The isotropic hyperfine interaction,  $A_{\text{iso}}$ , is positive and dominates over the dipolar contribution,  $T$ . As a result, the nuclear magnetic moment (brown arrow) is always anti-aligned with the electron magnetic moment (white arrows) (upper row in (b–d)) (note that the  $g$ -factors of both the electron and nuclear spins of Ti are negative). The anisotropic dipolar contribution, on the other hand, modifies the hyperfine strength depending on the direction of  $\mathbf{B}_{\text{ext}}$  (lower row in (b–d)). When  $\mathbf{B}_{\text{ext}}$  is applied along the O-O direction in (b), a positive dipolar term,  $T_{\text{O}}$ , adds to  $A_{\text{iso}}$  and is responsible for the largest hyperfine interaction along this principal axis.  $\mathbf{B}_{\text{ext}}$  applied along the Mg-Mg or  $\hat{z}$  direction results in a negative dipolar term that reduces the amplitude of the total hyperfine interaction along these directions.

see Figure 4a). With the magnetic field applied along the O-O direction, this electron spin distribution results in a positive dipolar term,  $T_O > 0$ , which adds to  $A_{\text{iso}}$  and is responsible for the largest hyperfine interaction along this principal axis (Figure 4b). A magnetic field applied along the Mg-Mg or out-of-plane direction results in a negative dipolar term that reduces the amplitude of the total hyperfine interaction along these directions (Figure 4c, d). Quantitatively, we note that the GIPAW results overestimate the polarization of the 4s shell resulting in a Fermi contact contribution that is too large ( $A_{\text{iso}} \approx 170$  MHz). Nevertheless, the correct trend of the hyperfine anisotropy is captured (Figure S7). The difference between our results and previously published DFT works for Ti on thin layers of MgO<sup>32,33</sup> stems from the presence of the Ag substrate as well as the hydrogenated state of Ti. Importantly, unlike an earlier experimental study<sup>17</sup> measured with a single-axis magnetic field, the combined use of vector-field ESR spectroscopy and atom manipulation here allows precise characterization of the full hyperfine tensor and hence an accurate description of the ground-state spin distribution. The experimental measurement of the hyperfine tensor, together with  $g$ -factor anisotropy, yields a remarkable precision in the determination of the electronic ground state of a single paramagnetic center.

In this work, we show how angle-dependent single-atom ESR-STM spectra enable the precise determination of the hyperfine anisotropy and hence ground-state electron distribution. By measuring at the nano-electronvolt energy resolution, the ESR-STM hyperfine spectroscopy adds a unique probe of local electronic structure to the toolbox of STM. We envision that various types of single spin centers can be probed in a similar fashion,<sup>10</sup> enabling the optimization of their quantum spin properties for future applications in spin-based quantum computing and quantum sensing.

While writing this manuscript, we became aware of a similar experiment performed in another group.<sup>34</sup> Overall, their results agree very well with those presented here.

## Acknowledgement

This work was supported by the Institute for Basic Science (Grant No. IBS-R027-D1).

## Supporting Information Available

Supporting experimental data and simulations are provided in the supplementary information.

## References

- (1) Berliner, L. J. *Spin labeling : theory and applications / edited by Lawrence J. Berliner*; Academic Press New York, 1976.
- (2) Lovchinsky, I.; Sanchez-Yamagishi, J. D.; Urbach, E. K.; Choi, S.; Fang, S.; Andersen, T. I.; Watanabe, K.; Taniguchi, T.; Bylinskii, A.; Kaxiras, E.; Kim, P.; Park, H.; Lukin, M. D. Magnetic resonance spectroscopy of an atomically thin material using a single-spin qubit. *Science* **2017**, *355*, 503–507.
- (3) Kane, B. E. A silicon-based nuclear spin quantum computer. *Nature* **1998**, *393*, 133–137.
- (4) Kalra, R.; Laucht, A.; Hill, C. D.; Morello, A. Robust Two-Qubit Gates for Donors in Silicon Controlled by Hyperfine Interactions. *Phys. Rev. X* **2014**, *4*, 021044.
- (5) Abobeih, M. H.; Randall, J.; Bradley, C. E.; Bartling, H. P.; Bakker, M. A.; Degen, M. J.; Markham, M.; Twitchen, D. J.; Taminiau, T. H. Atomic-scale imaging of a 27-nuclear-spin cluster using a quantum sensor. *Nature* **2019**, *576*, 411–415.
- (6) Zhao, N.; Honert, J.; Schmid, B.; Klas, M.; Isoya, J.; Markham, M.; Twitchen, D.;

- Jelezko, F.; Liu, R.-B.; Fedder, H.; Wrachtrup, J. Sensing single remote nuclear spins. *Nature Nanotechnology* **2012**, *7*, 657–662.
- (7) Rugar, D.; Budakian, R.; Mamin, H. J.; Chui, B. W. Single spin detection by magnetic resonance force microscopy. *Nature* **2004**, *430*, 329–332.
- (8) Doherty, M. W.; Manson, N. B.; Delaney, P.; Jelezko, F.; Wrachtrup, J.; Hollenberg, L. C. The nitrogen-vacancy colour centre in diamond. *Physics Reports* **2013**, *528*, 1–45.
- (9) Schirhagl, R.; Chang, K.; Loretz, M.; Degen, C. L. Nitrogen-Vacancy Centers in Diamond: Nanoscale Sensors for Physics and Biology. *Annual Review of Physical Chemistry* **2014**, *65*, 83–105, PMID: 24274702.
- (10) Zwanenburg, F. A.; Dzurak, A. S.; Morello, A.; Simmons, M. Y.; Hollenberg, L. C. L.; Klimeck, G.; Rogge, S.; Coppersmith, S. N.; Eriksson, M. A. Silicon quantum electronics. *Rev. Mod. Phys.* **2013**, *85*, 961–1019.
- (11) Baumann, S.; Paul, W.; Choi, T.; Lutz, C. P.; Ardavan, A.; Heinrich, A. J. Electron paramagnetic resonance of individual atoms on a surface. *Science* **2015**, *350*, 417–420.
- (12) Zhang, X.; Wolf, C.; Wang, Y.; Aubin, H.; Bilgeri, T.; Willke, P.; Heinrich, A. J.; Choi, T. Electron spin resonance of single iron phthalocyanine molecules and role of their non-localized spins in magnetic interactions. *Nature Chemistry* **2022**, *14*, 59–65.
- (13) Chen, Y.; Bae, Y.; Heinrich, A. J. Harnessing the Quantum Behavior of Spins on Surfaces. *Advanced Materials* **2022**, *n/a*, 2107534.
- (14) Lambe, J.; Jaklevic, R. C. Molecular Vibration Spectra by Inelastic Electron Tunneling. *Phys. Rev.* **1968**, *165*, 821–832.
- (15) Song, Y. J.; Otte, A. F.; Kuk, Y.; Hu, Y.; Torrance, D. B.; First, P. N.; de Heer, W. A.;

- Min, H.; Adam, S.; Stiles, M. D.; MacDonald, A. H.; Stroscio, J. A. High-resolution tunnelling spectroscopy of a graphene quartet. *Nature* **2010**, *467*, 185–189.
- (16) Delgado, F.; Fernández-Rossier, J. Inelastic Electron Tunneling Spectroscopy of a Single Nuclear Spin. *Phys. Rev. Lett.* **2011**, *107*, 076804.
- (17) Willke, P.; Bae, Y.; Yang, K.; Lado, J. L.; Ferrón, A.; Choi, T.; Ardavan, A.; Fernández-Rossier, J.; Heinrich, A. J.; Lutz, C. P. Hyperfine interaction of individual atoms on a surface. *Science* **2018**, *362*, 336–339.
- (18) Yang, K.; Willke, P.; Bae, Y.; Ferrón, A.; Lado, J. L.; Ardavan, A.; Fernández-Rossier, J.; Heinrich, A. J.; Lutz, C. P. Electrically controlled nuclear polarization of individual atoms. *Nature Nanotechnology* **2018**, *13*, 1120–1125.
- (19) Köhler, J.; Brouwer, A. C. J.; Groenen, E. J. J.; Schmidt, J. Single Molecule Electron Paramagnetic Resonance Spectroscopy: Hyperfine Splitting Owing to a Single Nucleus. *Science* **1995**, *268*, 1457–1460.
- (20) Kim, J.; Jang, W.-j.; Bui, T. H.; Choi, D.-J.; Wolf, C.; Delgado, F.; Chen, Y.; Krylov, D.; Lee, S.; Yoon, S.; Lutz, C. P.; Heinrich, A. J.; Bae, Y. Spin resonance amplitude and frequency of a single atom on a surface in a vector magnetic field. *Phys. Rev. B* **2021**, *104*, 174408.
- (21) Haynes, W. M.; Lide, D. R.; Bruno, T. J. *CRC handbook of chemistry and physics*; CRC press, 2016.
- (22) Natterer, F.; Patthey, F.; Brune, H. Quantifying residual hydrogen adsorption in low-temperature STMs. *Surface Science* **2013**, *615*, 80–87.
- (23) Yang, K.; Bae, Y.; Paul, W.; Natterer, F. D.; Willke, P.; Lado, J. L.; Ferrón, A.; Choi, T.; Fernández-Rossier, J.; Heinrich, A. J.; Lutz, C. P. Engineering the Eigenstates of Coupled Spin-1/2 Atoms on a Surface. *Phys. Rev. Lett.* **2017**, *119*, 227206.

- (24) Bae, Y.; Yang, K.; Willke, P.; Choi, T.; Heinrich, A. J.; Lutz, C. P. Enhanced quantum coherence in exchange coupled spins via singlet-triplet transitions. *Science Advances* **2018**, *4*, eaau4159.
- (25) Steinbrecher, M.; Rausch, R.; That, K. T.; Hermenau, J.; Khajetoorians, A. A.; Pothoff, M.; Wiesendanger, R.; Wiebe, J. Non-collinear spin states in bottom-up fabricated atomic chains. *Nature Communications* **2018**, *9*, 2853.
- (26) Seifert, T. S.; Kovarik, S.; Juraschek, D. M.; Spaldin, N. A.; Gambardella, P.; Stepanow, S. Longitudinal and transverse electron paramagnetic resonance in a scanning tunneling microscope. *Science Advances* **2020**, *6*, eabc5511.
- (27) Veldman, L. M.; Farinacci, L.; Rejali, R.; Broekhoven, R.; Gobeil, J.; Coffey, D.; Ternes, M.; Otte, A. F. Free coherent evolution of a coupled atomic spin system initialized by electron scattering. *Science* **2021**, *372*, 964–968.
- (28) Abragam, A.; Bleaney, B. *Electron paramagnetic resonance of transition ions*; OUP Oxford, 2012.
- (29) Mabbs, F. E.; Collison, D. *Electron paramagnetic resonance of d transition metal compounds*; Elsevier: Amsterdam, 1992.
- (30) Varini, N.; Ceresoli, D.; Martin-Samos, L.; Giroto, I.; Cavazzoni, C. Enhancement of DFT-calculations at petascale: Nuclear Magnetic Resonance, Hybrid Density Functional Theory and Car–Parrinello calculations. *Computer Physics Communications* **2013**, *184*, 1827–1833.
- (31) Giannozzi, P.; Baseggio, O.; Bonfà, P.; Brunato, D.; Car, R.; Carnimeo, I.; Cavazzoni, C.; de Gironcoli, S.; Delugas, P.; Ferrari Ruffino, F.; Ferretti, A.; Marzari, N.; Timrov, I.; Urru, A.; Baroni, S. Quantum ESPRESSO toward the exascale. *The Journal of Chemical Physics* **2020**, *152*, 154105.



- (32) Shehada, S.; dos Santos Dias, M.; Guimarães, F. S. M.; Abusaa, M.; Lounis, S. Trends in the hyperfine interactions of magnetic adatoms on thin insulating layers. *npj Computational Materials* **2021**, *7*, 87.
- (33) Tosoni, S.; Pacchioni, G. Magnetic nature and hyperfine interactions of transition metal atoms adsorbed on ultrathin insulating films: a challenge for DFT. *Phys. Chem. Chem. Phys.* **2022**, *24*, 15891–15903.
- (34) Farinacci, L.; Veldman, L. M.; Willke, P.; Otte, S. Experimental Determination of a Single Atom Ground State Orbital through Hyperfine Anisotropy. 2022; <https://arxiv.org/abs/2207.06037>.